A Novel MIMO Control for Interleaved Buck Converters in EV DC Fast Charging Applications

Lorenzo Ntogramatzidis, Stefania Cuoghi, Mattia Ricco, *Senior Member, IEEE*, Riccardo Mandrioli, *Graduate Student Member, IEEE*, and Gabriele Grandi, *Senior Member, IEEE*

***Abstract*— This brief proposes a new multiple input multiple output (MIMO) control for off-board electric vehicle (EV) dc fast chargers. The proposed feedback matrix design avoids multiple tuning of controllers in multiple and interconnected loops while improving the performance of interleaved dc buck converters over classical PI/PID controls. The innovative features of the presented strategy are the reference current monotonic tracking from any initial state of charge with an arbitrarily fast settling time and the fast compensation of both load variations and imbalances among the legs. Numerical results validate the performance improvements of the proposed discrete-time MIMO algorithm for interleaved buck converters over classical PI/PID controls. Full-scale hardware-in-the-loop (HIL) and scaled-down prototype experimental results prove the feasibility and effectiveness of the proposal.**

***Index Terms*— Buck converter, electric vehicle (EV), hardware-in-the-loop (HIL), interleaved converter, multiple input multiple output (MIMO) control.**

I. Introduction

A SIGNIFICANT stream of literature has flourished in the past few years aimed at developing compact, lightweight switch power supplies with higher efficiency, fast dynamics and zero steady-state error under parametric component uncertainties and load variations. The interleaved multiphase converter offers several advantages, such as a reduction of switching and conduction losses, a reduction of the size and weight of the converter, an improvement of the total current ripple, and an increase of the switching frequency by interleaving each phase current [1], [2]. Additional advantages include the low cost and the highly standardized parallel modules.

By contrast, the critical aspect of the interleaved technique is its current sharing control, which is strongly affected by the switch on resistance or inductance mismatches [3]. These are due to the unavoidable construction tolerances which are difficult to control by the manufacturer and to temperature variations during the operation of the converter legs. Clearly, when there is unequal current sharing, the losses and heat dissipation will become unbalanced. It follows that the control of this converter requires a different control action for each leg, depending on the variation of multiple sensed signals. Current sharing, then, is a primary requirement when interleaving multiple phases because it improves system performance: it minimizes transient response and thermal problems, [4], [5]. Among all the control methods available in the literature, multiple and interconnected PI/PID controllers are the most widely utilized, see [6], [7], and [8]. Generally, a primary controller computes the average duty cycle on the basis of the transfer function of the converter obtained by state-space averaging. A further group of secondary controllers compensates for the unbalances between one "master" leg and the remaining "slave" legs. The main limitation of the widespread PID-based control strategy is a lack of robustness in the presence of large disturbance and uncertainty [9]. Nonlinear sliding mode control has been proven to overcome this problem. However, more accurate values of the parameters and information on the state vector are required. In [10], the duty ratio generated by the sliding mode control is adjusted for each phase by PI controllers. By contrast, the main advantage of fuzzy controllers is that no prior knowledge of the converter is needed. However, fuzzy logic controllers require substantial computational power due to complex and heuristic decision-making processes, namely fuzzification, rule base storage, an inference mechanism, and process of defuzzification [11]. To overcome these limitations, in this brief we propose a new multiple input multiple output (MIMO) control algorithm based on the method introduced first in [12] and further developed in [13]. The key idea behind this approach, which goes under the name of *global monotonicity*, is to design the feedback matrix that guarantees a monotonic response from any initial condition (and therefore avoids overshoot and undershoot) with an arbitrarily fast settling time, by imposing a closed-loop eigenstructure where each component of the tracking error is driven only by a single real-valued closed-loop mode. It is proven in [13] that this is the only way in which the output of the system can be rendered monotonic in each output component regardless of the initial condition of the system.

The proposed MIMO control meets the current demand for new control strategies in the automotive sector for a reduction of greenhouse gas (GHG) emissions, as well as an

Manuscript received 15 December 2021; revised 14 August 2022; accepted 26 December 2022. Date of publication 24 January 2023; date of current version 22 June 2023. Recommended by Associate Editor G. Pin. *(Corresponding author: Riccardo Mandrioli.)*

Lorenzo Ntogramatzidis is with the School of Electrical Engineering, Computing and Mathematical Sciences, Curtin University, Perth, WA 6102, Australia (e-mail: l.ntogramatzidis@curtin.edu.au).

Stefania Cuoghi, Mattia Ricco, Riccardo Mandrioli, and Gabriele Grandi are with the Department of Electrical, Electronic and Information Engineering, University of Bologna, 40126 Bologna, Italy (e-mail: stefania.cuoghi4@unibo.it; mattia.ricco@unibo.it; riccardo.mandrioli4@unibo.it; gabriele.grandi@unibo.it).

Color versions of one or more figures in this article are available at https://doi.org/10.1109/TCST.2023.3237497.

Digital Object Identifier 10.1109/TCST.2023.3237497

improvement of the quality of urban air [14]. In particular, electric vehicles (EVs) powered by batteries and recharged with electricity from renewable sources allow for a reduction of emissions by up to 30% compared to a car with a thermal engine [15]. Battery technology plays a key role in the diffusion of EVs, due to the significant correlation between battery cost, lifetime, charging time, and the characteristics of the employed battery charger, [16]. Battery chargers can be classified into three main power levels. In particular, level three refers to the fast chargers. This type of chargers is off-board, generally installed in public charging stations, and supplies high dc power directly to the battery. The major challenges for these chargers are the cost reduction and the competitiveness of the charge time against the conventional petroleum refill [17], [18], [19]. Several converter topologies have been proposed in the literature to meet these targets, including the Vienna rectifier [20], and the multilevel neutral point clamped (NPC) converter [21]. The buck converter is widely used in the dc–dc charger stage for its simple structure and well-known design procedures. Generally speaking, the Lithium-ion (Li-ion) battery charging strategy can be divided into three classes as follows:

1) Empirical model-oriented charging controls, which predict the battery states and calculate electrical elements using past experimental data. In these cases, the battery charging can be improved by fuzzy control, linear quadratic control, or model predictive control.
2) Control algorithms based on electrochemistry battery models aimed at minimizing the charging time while performing thermal management of the battery.
3) Model-free methods, including constant-current (CC), CC constant-voltage (CCCV), multistage CCCV, and pulse charging techniques.

The main advantages and drawbacks of these control algorithms are discussed in [22], [23], and [24]. Right now, the most common EV charging method is the CC-CV [25]. The performance of the proposed MIMO control has been experimentally verified and compared against other methods via simulations. The main features of this converter control for EV dc fast charging are as follows.

1) The design of a MIMO control system avoids multiple tuning of PI/PID controllers in multiple and interconnected loops.
2) The system matrix of the interleaved buck converter has two complex conjugate eigenvalues, while the eigenvalues of the controlled system matrix are all real and stable.
3) A real-time procedure controls the steady-state values of the state variables, but the feedback matrix determines the dynamic behavior of the system.
4) A monotonic tracking error decay is guaranteed from any initial condition (and this in turn ensures a non-overshooting and non-undershooting response from any initial state).
5) The procedure has a degree of freedom that can be tuned to impose the reference current step response settling time.

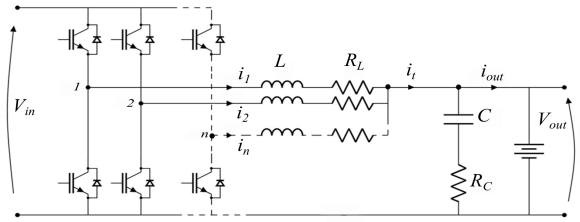

Fig. 1. N-leg interleaved buck converter for EV fast charging applications.

6) The closed-loop system compensates for variations of the set-point current/load and current imbalances among the legs under variations of the system parameters.

The brief is organized as follows. Section II presents the discrete-time state-space model of the power converter. The tracking control problem and the description of the proposed n-leg interleaved buck converter control are presented in Sections III and IV, respectively. Section V presents a comparison with other methods while in Section VI numerical, real-time, and experimental results obtained using a Li-ion rechargeable battery pack are provided. In the last section, the conclusion derived from this work is drawn.

II. Interleaved Buck Converter Circuit and Discrete-Time State-Space Model

Standard off-board EV chargers are composed of an ac–dc converter used as a power grid interface followed by a dc–dc converter that controls the battery charging process.

The dc–dc converter considered in this brief is an n-leg interleaved buck converter as shown in Fig. 1. Here, V_{in} represents the input voltage, (dc-link voltage), while i_{out} and V_{out} denote the output current and voltage, respectively.

Each leg includes a power stage composed of two insulated-gate bipolar transistors (IGBTs) switches with on-state resistance R_{Sw}, and an inductor with inductance L and coupling resistance R_L. The equivalent series resistances (ESRs) in each j-leg are given by

$$R_{\text{sj}} = R_{\text{Swj}} + R_{\text{Lj}}, \quad j = 1, 2, \ldots, n. \tag{1}$$

The power switches are toggled by pulse-width modulation (PWM) signals shifted by $360°/n$ from each other and with duty cycles $d_1(k), d_2(k), \ldots, d_n(k) \in [0, 1]$ to be designed. The filter capacitance C with parasitic series resistance R_C is shared by the phases. Assuming a low capacitor ESR, the effects introduced by R_C can be neglected, and the output voltage can be approximated to V_C, while the output current i_{out} can be approximated to the total current as

$$i_t(k) = \sum_{j=1}^{n} i_j(k) \approx i_{\text{out}}. \tag{2}$$

The discrete-time state-space model of the interleaved buck converter can be written as

$$\Sigma : \begin{cases} x(k+1) = A\,x(k) + B\,u(k), & x(0) = x_0 \\ y(k) = C\,x(k) \end{cases} \tag{3}$$

where the vectors

$$x(k) = \begin{bmatrix} i_1(k) \\ \vdots \\ i_n(k) \\ V_C(k) \end{bmatrix}, \quad u(k) = \begin{bmatrix} d_1(k) \\ \vdots \\ d_n(k) \end{bmatrix}, \quad y(k) = \begin{bmatrix} i_1(k) \\ \vdots \\ i_n(k) \end{bmatrix} \tag{4}$$

represent, respectively, the m-dimensional state (with $m = n+1$), the n-dimensional control input (which has duty-cycle signals as components), and the n-dimensional output. Thus, $A \in \mathbb{R}^{m\times m}$, $B \in \mathbb{R}^{m\times n}$, $C \in \mathbb{R}^{n\times m}$, are the system matrix, the input matrix, and the output matrix, respectively. These matrices can be obtained by the continuous-time state-space model of the interleaved buck converter, see [8], using a zero-order hold discretization method and sampling time T_s.

III. Global Monotonic Tracking

Global monotonic tracking refers to the problem of designing a state-feedback control law for a MIMO linear time-invariant system such that for all initial conditions the output y tracks a step reference r with zero steady-state error and is monotonic in all components. If y asymptotically tracks the constant reference r and is monotonic, then it is also both non-overshooting and non-undershooting.

If the discrete-time system is right invertible and stabilizable, and has no invariant zeros at 1 (these are the standard assumptions for a tracking problem to be solvable, see, e.g., [26]), given the step reference r to track, we proceed as follows: first, we choose a feedback gain matrix F such that $A + B\,F$ is asymptotically stable. We then choose two steady-state vectors $x_{\rm ss}$ and $u_{\rm ss}$ that, for the given r, satisfy the linear equation

$$x_{\rm ss} = A\,x_{\rm ss} + B\,u_{\rm ss}, \qquad r = C\,x_{\rm ss}. \tag{5}$$

This equation always admits a solution

$$\begin{bmatrix} x_{\rm ss} \\ u_{\rm ss} \end{bmatrix} = \begin{bmatrix} A - I & B \\ C & 0 \end{bmatrix}^{-1} \begin{bmatrix} 0 \\ r \end{bmatrix}$$

in view of the right-invertibility and the absence of eigenvalues of A at 1 (this latter assumption implies that $A - I$ is invertible). Now, applying the state-feedback control law

$$u(k) = F\left(x(k) - x_{\rm ss}\right) + u_{\rm ss} \tag{6}$$

to (3) and using the change of variable $\xi = x - x_{\rm ss}$ gives the closed-loop autonomous system

$$\Sigma_{\rm aut}: \begin{cases} \xi(k+1) = (A + B\,F)\,\xi(k), & \xi(0) = x_0 - x_{\rm ss} \\ y(k) = C\,\xi(k) + r. \end{cases} \tag{7}$$

The dynamics of the closed-loop system are governed by the eigenvalues of $A + B\,F$: the uncontrollable eigenvalues are stable from the assumption of stabilizability, while the other eigenvalues can be assigned arbitrarily to be stable and sufficiently fast to improve the speed of the response. Since $A + B\,F$ is asymptotically stable, x converges to $x_{\rm ss}$, ξ converges to zero and y converges to r as t goes to infinity.

Our goal is to select F in such a way that global monotonicity is guaranteed from any initial condition, and this is possible if and only if we can ensure that the tracking error $\epsilon(k) = y(k) - r(k)$ converges monotonically to 0 in all components, from all initial conditions. This is in turn equivalent to requiring the tracking error to have the structure

$$\epsilon(t) = \left[\beta_1\,\lambda_1^k, \ldots, \beta_n\,\lambda_n^k\right]^T \tag{8}$$

where $\lambda_1, \ldots, \lambda_n$ are closed-loop eigenvalues (and they are therefore stable). In other words, if we are able to obtain a tracking error $\epsilon(t)$ that consists of a single power per component and $|\lambda_k| < 1$, the problem is solved since the powers of λ_k are monotonic functions of k. The converse is also true: the only way to obtain a feedback matrix ensuring global monotonic tracking is to obtain a tracking error as in (8): hence, in order for the problem of global monotonic tracking to be solvable, we need to distribute (at most) n modes evenly into the tracking error with one mode per error component. To achieve this goal, all the remaining closed-loop modes have to be made invisible from the tracking error. The task is now to find F such that for every ξ_0 the error $\epsilon(k)$ is given by a single stable real mode per component. Let $j = 1, \ldots, n$. Let $\lambda_j \in (-1, 1)$. Consider a solution v_j and w_j of the linear equation

$$\begin{bmatrix} A - \lambda_j\,I & B \\ C & 0 \end{bmatrix} \begin{bmatrix} v_j \\ w_j \end{bmatrix} = \begin{bmatrix} 0 \\ \beta_j\,e_j \end{bmatrix} \tag{9}$$

where $\beta_j \neq 0$ and e_j is the jth vector of the standard basis of $\mathbb{R}^n$: (9) always has a solution in view of the right-invertibility of the system. By choosing F such that $F\,v_j = w_j$, we find $(A + B\,F)\,v_j = \lambda_j\,v_j$ and $C\,v_j = \beta_j\,e_j$. Hence, for any $\xi_0 \in \text{span}\{v_j\}$ the response is

$$\epsilon(k) = e_j \gamma_j\,\lambda_j^k \tag{10}$$

where γ_j depends on ξ_0. Considering $\lambda_1, \ldots, \lambda_n \in (-1, 1)$; by applying this argument for all components of the tracking error, we obtain a set of solutions $\left[\begin{smallmatrix} v_1 \\ w_1 \end{smallmatrix}\right], \left[\begin{smallmatrix} v_2 \\ w_2 \end{smallmatrix}\right], \ldots, \left[\begin{smallmatrix} v_n \\ w_n \end{smallmatrix}\right]$ of (9). If $v_1, \ldots, v_n$ are linearly independent, we can choose F to be such that $F\,v_i = w_i$ for all $i = 1, \ldots, n$. Then, for every $\xi_0 \in \text{span}\{v_1, v_2, \ldots, v_n\}$, by superposition we find

$$\epsilon(k) = \begin{bmatrix} \gamma_1\,\lambda_1^k \\ 0 \\ \vdots \\ 0 \end{bmatrix} + \begin{bmatrix} 0 \\ \gamma_2\,\lambda_2^k \\ \vdots \\ 0 \end{bmatrix} + \begin{bmatrix} 0 \\ 0 \\ \vdots \\ \gamma_n\,\lambda_n^k \end{bmatrix} = \begin{bmatrix} \gamma_1\,\lambda_1^k \\ \gamma_2\,\lambda_2^k \\ \vdots \\ \gamma_n\,\lambda_n^k \end{bmatrix}. \tag{11}$$

For this response to be achievable from any initial condition, we also need to render the remaining $m-n$ closed-loop modes invisible at ϵ. This task can be accomplished by exploiting the supremal stabilizability output-nulling subspace $\mathcal{V}_g^\star$ of the system. This subspace can be obtained as the image of $[\,V_1 \;\; V_2 \;\; \cdots \;\; V_d\,]$ that satisfies

$$\begin{bmatrix} A - \mu_j\,I & B \\ C & 0 \end{bmatrix} \begin{bmatrix} V_j \\ W_j \end{bmatrix} = 0 \tag{12}$$

for some other matrix $[\,W_1 \;\; W_2 \;\; \cdots \;\; W_d\,]$ partitioned conformably, where $\{\mu_1, \ldots, \mu_t\}$ are the minimum-phase invariant zeros of Σ and $\{\mu_{t+1}, \ldots, \mu_d\}$ are arbitrary and stable (assume, e.g., that they are real and distinct for simplicity). If the dimension of $\mathcal{V}_g^\star + \text{span}\{v_1, v_2, \ldots, v_n\}$ is equal to m, every initial state ξ_0 can be decomposed as the sum $\xi_v + \xi_r$,

where $\xi_v \in \mathcal{V}_g^\star$ and $\xi_r \in \text{span}\{v_1, v_2, \ldots, v_n\}$. If $\dim \mathcal{V}_g^\star = m-n$, and we can find a set of linearly independent columns $\{v_{n+1}, \ldots, v_m\}$ from the columns of $[\,V_1 \;\; V_2 \;\; \cdots \;\; V_d\,]$ that is linearly independent of $\{v_1, \ldots, v_n\}$, we can take $w_{n+1}, \ldots, w_m$ to be the columns of W_g that correspond to $v_{n+1}, \ldots, v_m$, and construct the feedback control $\omega(k) = F\,\xi(k)$ where F is such that $F\,[\,v_1 \;\; \cdots \;\; v_n \;\; v_{n+1} \;\; \cdots \;\; v_m\,] = [\,w_1 \;\; \cdots \;\; w_n \;\; w_{n+1} \;\; \cdots \;\; w_m\,]$, the response associated with ξ_v is identically zero, while the one associated with ξ_r is still given by (11). Hence, the tracking error can be written as in (8) for any ξ_0. The closed-loop eigenvalues obtained with F are given by the union of $\{\lambda_1, \ldots, \lambda_n\}$, with the set of μ_j associated with the columns $\{v_{n+1}, \ldots, v_m\}$ chosen from $[\,V_1 \;\; V_2 \;\; \cdots \;\; V_d\,]$.

IV. Interleaved Buck Converter MIMO Control

One of the available and widely adopted Li-ion battery charging strategies is the CCCV technique. This approach reduces the negative effects on the performance in both the converter and the battery caused by voltage and current spikes, by selecting a charging profile composed of two main modes. A constant current control mode leads to fast charging up to high values of SOCs and for this reason it is predominant in EV dc fast charging facilities. Then, the charging current can eventually gradually decrease under constant voltage control up to the final value of the output current [22]. Focusing on the constant current control mode, the proposed method hinges on the implementation of two distinct control algorithms to satisfy the specifications (zero steady-state tracking error under the reference signal i_t^*, asymptotic stability and nonovershooting/nonundershooting dynamics). The first algorithm calculates the steady-state values of the state and control vectors x_{ss} and u_{ss} during the battery charging process, as functions of the reference current i_t^*, the open circuit battery voltage V_{OC}, the battery droop coefficient R and the leg resistances (1). It can be easily shown that [22]

$$x_{\text{ss}} = \begin{bmatrix} \frac{i_t^*}{n} \\ \frac{i_t^*}{n} \\ \frac{i_t^*}{n} \\ i_t^* R + V_{\text{OC}} \end{bmatrix}, \quad u_{\text{ss}} = \begin{bmatrix} \frac{V_{\text{OC}} + i_t^*\left(R + \frac{R_{s1}}{n}\right)}{V_{\text{in}}} \\ \frac{V_{\text{OC}} + i_t^*\left(R + \frac{R_{s2}}{n}\right)}{V_{\text{in}}} \\ \frac{V_{\text{OC}} + i_t^*\left(R + \frac{R_{s3}}{n}\right)}{V_{\text{in}}} \end{bmatrix} \tag{13}$$

where the real-time droop coefficient R of the battery and the steady-state leg resistance R_{sj} are computed as

$$R = \frac{V_{\text{out}} - V_{\text{OC}}}{i_{\text{out}}}, \quad R_{\text{sj}} = \frac{V_{\text{in}} d_j - V_{\text{out}}}{i_j}.$$

The open-circuit voltage can be estimated, for example, on the basis of the battery state of charge SOC using the lookup table method [27], [28].

The second control algorithm implements the discrete control law (6). In particular, the constant gain matrix F is designed using the global monotonic tracking method described in Section III. The corresponding control system is depicted in Fig. 2.

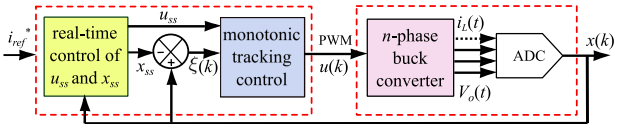

Fig. 2. Block diagram comprising converter and control scheme.

TABLE I
Parameter Values of the Interleaved Buck Converter Circuit

Symbol	Parameter	a) Simulation/HIL	b) Experiment
n	Number of legs	3	3
L	Filter Inductance	344 μH	680 μH
C	Filter Capacitance	16.0 μF	100 μF
R_L	Inductor ESR	300 mΩ	173 mΩ
R_{Sw}	Leg ESR	20 mΩ	70 $m\Omega$
V_{in}	DC-Input voltage	618 V	24.0 V
i_t^*	Output ref. current	125 A	2.50 A
f_{sw}	Switching freq.	20 kHz	20 kHz
f_s	Sampling freq.	60 kHz	60 kHz
A/D	ADC resolution	12 bit	12 bit

The interleaved modulation adopted in this brief is described in detail in [4]. Samplings are performed at the peak of each PWM carrier; this leads to a current value equal to the average inductor current (no current ripple detection), see [8]. It follows that an interrupt routine is generated at the sampling frequency $f_s = n \cdot f_{\text{sw}}$, where f_{sw} is the PWM switching frequency. Each sampled current is stored and used to update the n duty cycles. Therefore, with three interleaved legs and a 20 kHz switching frequency, the sampling frequency is equal to 60 kHz (3 · 20 kHz).

V. Comparison With Conventional PI and PIDF

Several tests have been considered to evaluate the performance of the proposed method under parameter variations and model uncertainties in comparison with PI/PIDF average controls described in [6] and [8] with reference to Table Ia) full-scale scenario with a 3.84 Ω resistive load. In these current-balance controls the average duty cycle is computed by a primary controller on the basis of the converter averaging model. Secondary PI controllers calculate the duty ratio to compensate for the unbalances between the legs. In particular, in [8] a direct digital design method for discrete controllers with PID structure + filter, therein referred to as PIDF controllers, is introduced. This method is based on a pole-zero cancellation technique jointly with an analytical design technique based on "inversion formulae," which explicitly express the parameters of the controller in terms of the design specifications given by the phase/gain margins and the corresponding crossover frequencies, see [29]. For a fair comparison, the PI controller $PI = K_p + K_i(T_s/(z-1))$ using the control strategy described in [6] has been designed to get a monotonic response. In particular, the values $K_p = 0.15e^{-3}$ and $K_i = 18.16$ lead to a phase margin of 71° and a gain crossover frequency of 3000 rad/s. These are the same design specifications given for the PIDF tuning, see [29].

The state-space model of the buck converter is characterized by the following discrete-time system matrices:

$$A = \begin{bmatrix} 0.9620 & -0.0226 & -0.0226 & -0.0410 \\ -0.0226 & 0.9620 & -0.0226 & -0.0410 \\ -0.0226 & -0.0226 & 0.9620 & -0.0410 \\ 0.8823 & 0.8823 & 0.8823 & 0.7002 \end{bmatrix}$$

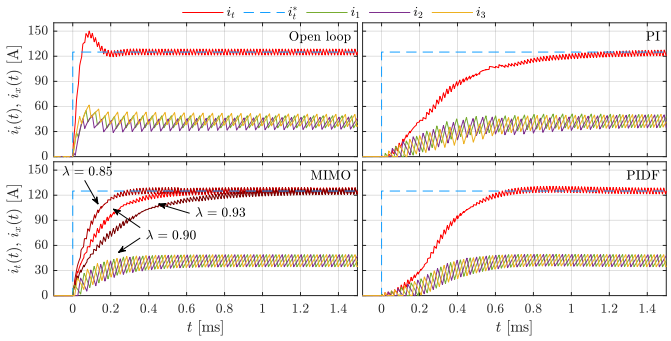

Fig. 3. Step responses using duty cycles $d_{1,2,3} = 79.8\%$ in open loop, PI/PIDF average control strategies (see [6], [8]), and proposed MIMO global monotonic tracking method.

$$B = \begin{bmatrix} 29.511 & -0.2326 & -0.2326 \\ -0.2326 & 29.511 & -0.2326 \\ -0.2326 & -0.2326 & 29.511 \\ 14.040 & 14.040 & 14.040 \end{bmatrix}, \quad C = \begin{bmatrix} 1 & 0 & 0 & 0 \\ 0 & 1 & 0 & 0 \\ 0 & 0 & 1 & 0 \end{bmatrix}$$

with zero initial condition. This system is completely reachable, and it is therefore stabilizable. Moreover, a direct computation shows that it is right invertible,[1] and it has a minimum-phase invariant zero at 0.7597.

The steady-state values of the state variables and control signals are dynamically calculated using (13). These are equal to $x_{ss} = [41.66\ 41.66\ 41.66\ 480.0]^\top$ and $u_{ss} = [0.798\ 0.798\ 0.798]^\top$, respectively. The global monotonic tracking method has been applied to the design of the gain matrix F that achieves a globally monotonic response. In particular, since $m-n=1$, the first eigenvalue of the closed-loop system has been selected to be equal to the invariant zero of the system to be controlled, $\lambda_1 = 0.7597$. The values of the other three eigenvalues λ_2, λ_3 and λ_4 have been chosen in the stability unit circle and are equal to each other to keep a converter leg balanced current sharing. The value of $\lambda \in [0, 1)$ is a degree of freedom of the control and can be chosen to achieve a desired settling time in the step response. Setting this value equal to $\lambda = 0.90$, the corresponding feedback gain matrix is

$$F = 10^{-4} \begin{bmatrix} -20.89 & 7.550 & 7.550 & 14.14 \\ 7.550 & -20.89 & 7.550 & 14.14 \\ 7.550 & 7.55. & -20.89 & 14.14 \end{bmatrix}.$$

The step responses of the inductor currents and the total current obtained with constant duty cycles at 79.8% in an open loop and obtained with the three considered methods are shown in Fig. 3. In all cases the requirement of zero tracking error is satisfied. As expected, the advantage of the proposed solution is a faster response, by 58% and 41% compared to the PI and PIDF controller, respectively. Moreover, the settling time can be modified simply by changing the value of λ as a degree of freedom; $\lambda = 0.9$ leads to a settling time equal to 1.2 ms. In Fig. 3, different settling times are presented for the values $\lambda \in \{0.85, 0.90, 0.93\}$. A physical limitation on the velocity of the step response is given by the imposition of the duty cycles to be in the interval $[0, 1]$ in (4).

[1]To this end, it suffices to verify that the sum of the supremal controlled invariant subspace contained in the null-space of C and the infimal conditioned invariant subspace containing the image of B is the entire state space.

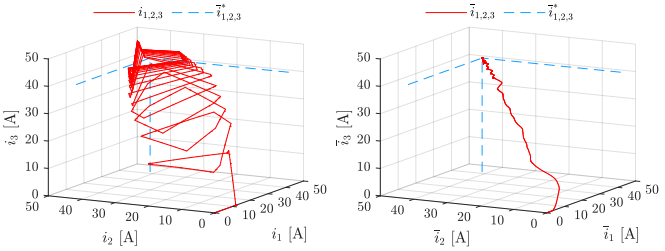

Fig. 4. State-space trajectories of the instantaneous (left) and averaged (right) interleaved currents using global monotonic tracking control.

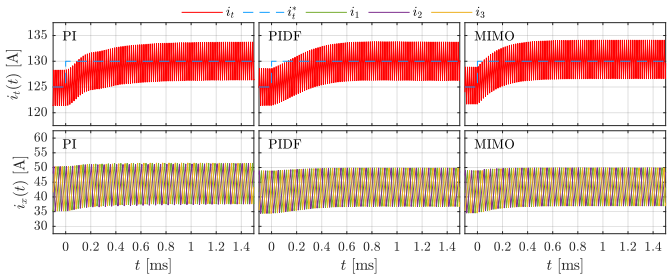

Fig. 5. Set point i_t^* variation from 125 to 130 A using PI, PIDF, and global monotonic tracking methods.

TABLE II
LI-ION BATTERY PARAMETERS

Symbol	Parameter	a) Simulation/HIL	b) Experiment
V_n	Nominal voltage	477 V	4×3.70 V
C_r	Rated capacity	50 Ah	2.5 Ah
T_r	Response time	30 s	-
V_c	Cut-in voltage	555 V	16.8 V
V_d	Cut-out voltage	-	4×4.20 V
R_i	Internal resistance	95 mΩ	-
V_e	Exponential voltage	515 V	-
C_e	Exponential capacity	2.46 Ah	-

The state-space trajectories of the averaged inductor currents at steady-state converge as shown in Fig. 4 (right). The instantaneous currents stabilize over a closed path, whose area is related to peak-to-peak ripple of the current, see Fig. 4 (left).

Results for a step-type variation of $i_t^*(t)$ from the nominal value 125–130 A are shown in Fig. 5. The controls guarantee zero tracking error in all the considered cases. The method presented in this brief leads to the fastest response: 0.3 s compared to 0.6 and 0.5 s of PI and PIDF controls.

VI. NUMERICAL AND EXPERIMENTAL VALIDATION

The proposed MIMO control structure has been tested numerically, in real-time hardware-in-the-loop (HIL), and experimentally employing the converter parameters in Table I and the battery models in Table II. In particular, the values in Tables Ia) and IIa) represent a full-scale scenario chosen for comparative analysis against other methods and for the real-time HIL validation, while the values in Tables Ib) and IIb) refer to the scaled-down experimental prototype.

A. Numerical Results Based on Shepherd's Li-Ion Battery Model

Numerical simulation results have been acquired using the MATLAB-Simulink (MathWorks) battery block, in which

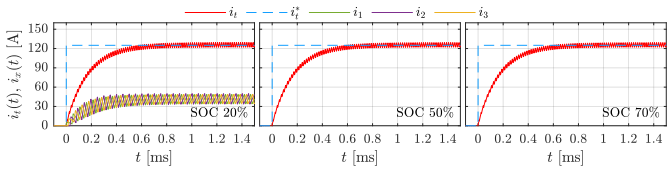

Fig. 6. Shepherd's battery model step responses with multiple initial SOC.

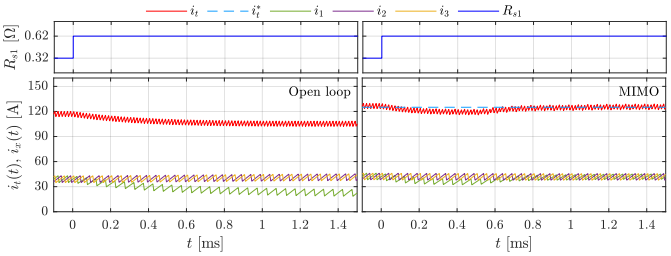

Fig. 7. Responses under step variation of R_{s1} from 0.32 to 0.62 Ω of the open-loop system versus the proposed MIMO control.

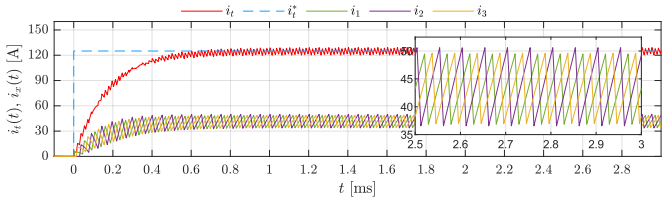

Fig. 8. Proposed method step response with an L_2 10% inductor reduction.

the battery is modeled based on the Shepherd's model with parameters given in Table II [30]. The control is implemented using the same feedback gain matrix F discussed in Section V.

The results shown in Fig. 6 refer to a step variation of i_t^* from 0 to 125 A, $\lambda = 0.85$ in the case of SOC equal to 20%. The chosen reference current corresponds to a charging rate of 2.5 C likely in low-SOC battery packs connected to fast charging facilities. The currents monotonically track the reference value $i_t^*/3$ with zero steady state error in 0.5 ms. Moreover, to test if this result is obtained from any initial condition, simulations have been carried out from SOC 20% and 70%. In all the cases, the tracking error vanishes monotonically.

The control of the output current and inductor currents under variations of R_{s1} are shown in Fig. 7. At $t = 0$ ms, the resistance of the first leg series has been modified from 0.32 to 0.62 Ω. The current balancing among the legs has been reached in 0.7 ms, confirming that the control compensates for resistance variations among the legs in contrast with the open-loop scenario.

Finally, simulations have been carried out to evaluate the robustness of the proposed control method under uncertainties on the value of the inductor—inductors are among the components with highest nominal value uncertainty. In particular, Fig. 8 shows the total and inductor currents under variations of the reference step when $L_2 = 0.9\ L$. Despite the dissymmetry in the peak-to-peak ripples of the inductor current, the total current mean value tracks the reference signal without steady-state error in about 0.8 ms.

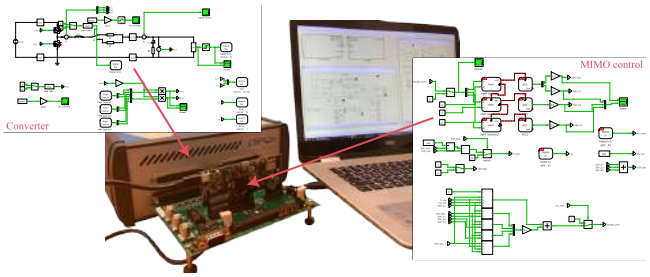

Fig. 9. Real-time HIL experimental setup.

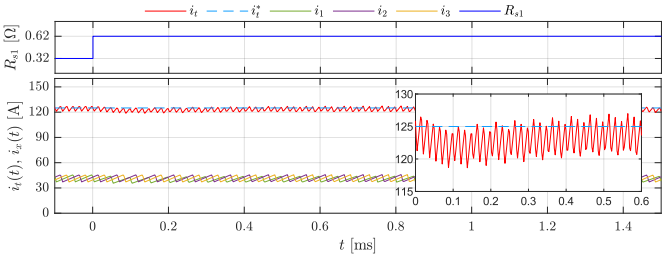

Fig. 10. HIL responses under step variation of R_{s1} from 0.32 to 0.62 Ω of the proposed MIMO control.

B. HIL Real-Time Validation

To validate the real-time feasibility, HIL results have been acquired employing the experimental setup in Fig. 9. The full-scale converter plant [Table Ia)] was emulated in real-time inside the RT-Box 1 (Plexim) while the TMS320F28379D (Texas Instruments) digital signal processor (DSP) run the controller on a separated control card. Both RT-Box 1 and DSP execution codes have been deployed in a PLECS (Plexim) environment and the results have been collected using the external mode functionality. This test allows one to verify the feasibility of a commercial DSP with actual execution times, PWMs generation synchronization, and sensing/conversion delays. The full-scale converter has been emulated with a 2.38 μs discretization step and using the same battery parameters of Section VI-A [see Table IIa)] with 50% initial SOC, which accounts for all the main phenomena tackled by a real full-scale prototype. The control is implemented using the same feedback gain matrix F as in Section V.

Similar to what was done for our simulation results, the step response, the current balancing, and the robustness under parameter uncertainty have been verified. The same R_{s1} step shown in Section VI-A is visible in Fig. 10; the real DSP restores the HIL current balancing in about 0.6 ms instead of 0.7 ms as visible in Fig. 7.

Fig. 11 shows the HIL step response under inductor uncertainty ($L_2 = 0.9L$). Other than a slightly different current ripple peak-to-peak range, no average current drift/mismatch is observed. The proposed MIMO control guarantees a monotonic tracking response in about 0.6 ms.

C. Experimental Validation on a Scaled-Down Prototype

The performance of the proposed MIMO control for the dc charger has been evaluated using the set-up shown in Fig. 12. In particular, the three-phase interleaved buck converter is

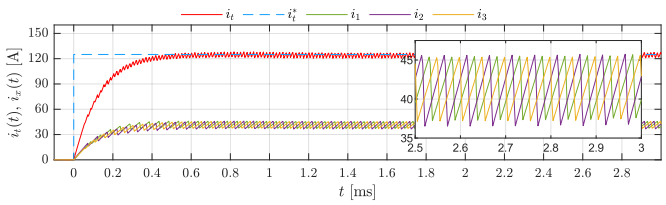

Fig. 11. Proposed method HIL step response with an L_2 10% inductor reduction.

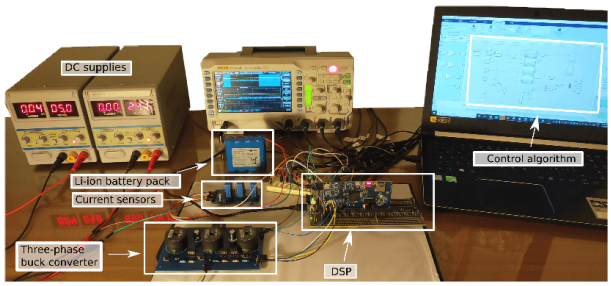

Fig. 12. Scaled-down experimental setup.

characterized by the parameters shown in Tables Ib) and IIb). The currents of the inductors have been detected by three LES 6-NP (LEM) Hall effect current sensors which guarantee galvanic isolation between the converter power board and the DSP side. The output signals of the current sensors are proportional to the sensed current except for a 2.5 V offset. A dedicated conditioning circuit has been designed to interface with the 3.3 V 12-bit analog-to-digital converter (ADC) of the DSP control card. The same DSP used for HIL results generates the PWM signals to drive the bipolar junction transistors (BJTs) of the converter. The battery is a Li-ion rechargeable pack consisting of four 18650 cells having nominal voltage 3.7 V each [see Table IIb)]. This kind of battery cell is widely employed in high-performance battery packs from first-tier EV manufactures (e.g., Tesla Inc.). The proposed MIMO control has been implemented in MATLAB/Simulink, then the executable C code has been deployed to the DSP target employing Code Composer Studio (Texas Instruments) IDE. Experimental results have been acquired using the oscilloscope DS1054Z (Rigol) at a sampling rate ranging from 5 to 250 MSa/s.

The model of the experimental converter with zero initial condition is characterized by the matrices

$$A = \begin{bmatrix} 0.992 & -0.002 & -0.002 & -0.024 \\ -0.002 & 0.992 & -0.002 & -0.024 \\ -0.002 & -0.002 & 0.992 & -0.024 \\ 0.163 & 0.163 & 0.163 & 0.966 \end{bmatrix}$$

$$B = 10^{-4} \begin{bmatrix} 5861 & -3.969 & -3.969 \\ -3.969 & 5861 & -3.969 \\ -3.969 & -3.969 & 5861 \\ 484.0 & 484.0 & 484.0 \end{bmatrix}, \quad C = \begin{bmatrix} 1 & 0 & 0 & 0 \\ 0 & 1 & 0 & 0 \\ 0 & 0 & 1 & 0 \end{bmatrix}.$$

The experimental currents of the inductor and the output voltage at steady-state correspond to the expected state/input variables $x_{ss} = [0.8333\ 0.8333\ 0.8333\ 14.80]^\top$ and $u_{ss} = [0.625\ 0.625\ 0.625]^\top$. The proposed method has been then applied to the experimental converter to achieve a globally monotonic response. In particular, the first eigenvalue of the closed-loop system has been selected to be equal to the invariant zero of the system to be controlled, while the values of the other three eigenvalues have been chosen in the stability unit circle and equal to each other in order to keep a balanced current share among the converter legs. Setting these values equal to $\lambda \in \{0.972, 0.985, 0.985, 0.985\}$, the feedback gain matrix is

$$F = 10^{-4} \begin{bmatrix} -118 & 34.3 & 34.3 & 411 \\ 34.3 & -118 & 34.3 & 411 \\ 34.3 & 34.3 & -118 & 411 \end{bmatrix}.$$

Test results under step responses from V_{OC} equal to 13.5 V using a open-loop strategy with duty cycle $d = 62.5\%$ and the proposed MIMO global monotonic tracking method with $\lambda = 0.985$ and $i_t^* = 2.5$ A (1C charging rate) are shown in Fig. 13 (top and bottom frames, respectively). Notice that the steady-state value $i_t^*/3$ of the inductor currents are monotonically tracked, while the open-loop control leads to current overshoot with magnitude twice the required values and a steady state value about 20% lower than the expected one. This open-loop mismatch is due to multiple nonideal parameters such as the BJT voltage drop, unaccounted losses, and so

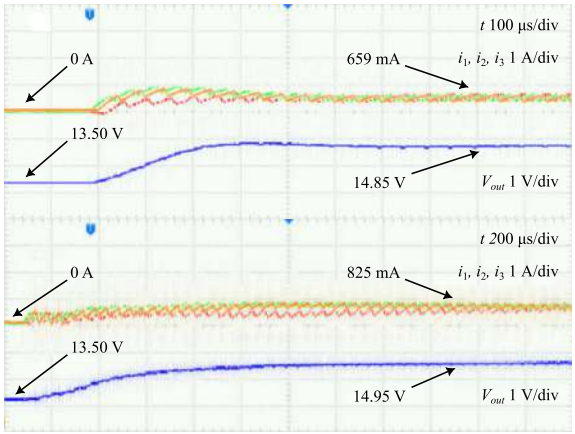

Fig. 13. Step responses using Li-ion battery pack from $V_{OC} = 13.5$ V in open-loop (top) with duty cycle equal to 62.5% and the proposed MIMO global monotonic tracking methods with $i_t^* = 2.5$ A (bottom).

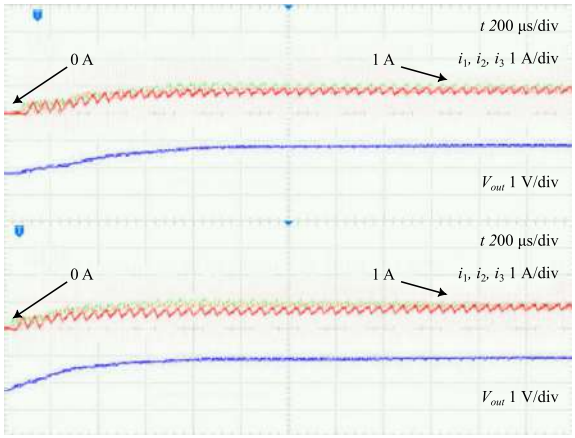

Fig. 14. Step responses using Li-ion battery pack with $i_t^* = 3$ A, $\lambda = 0.985$ (top) and $\lambda = 0.980$ (bottom).

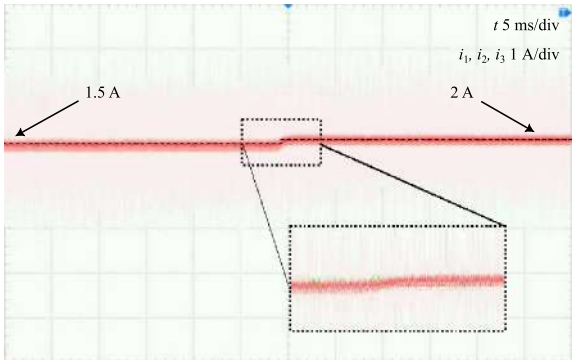

Fig. 15. Inductor currents under +33% i_t^* step variation from 1.5 to 2 A.

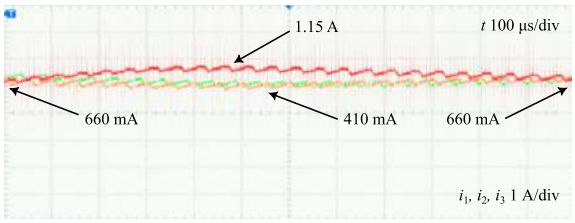

Fig. 16. Proposed control during a 1.5 Ω R_{s1} variation with $i_t^* = 2$ A.

on. The MIMO control strategy compensates for real system phenomena leading to the desired value in about 1.1 ms.

The global monotonic tracking method has been tested under step variations of i_t^* from 0 to 3 A with $\lambda = 0.985$ and $\lambda = 0.980$, see Fig. 14 (top) and (bottom) frames, respectively. Similar to what can be observed in Fig. 3, a smaller value of λ leads to a faster response. In this particular case, $\lambda = 0.985$ leads to a settling time of 1.1 ms, while $\lambda = 0.98$ leads to a value of 1 ms. Again, the steady state is reached without any overshoot.

The interleaved currents, under a variation of the set point i_t^* from 1.5 to 2 A, are shown in Fig. 15. The +33% current increment that can be observed is likely to occur in large EV charging facilities when power reallocation after the EV disconnection takes place [31]. Notice that the proposed MIMO control reaches the steady-state value without oscillations in less than 1 ms.

Finally, the proposed method has been also tested under variation of R_{s1}, by reducing its initial value by 1.5 Ω. The imbalanced current shared among the legs has been compensated in 1.2 ms, see Fig. 16. During the evolution, i_1 rises by about 74%, reaching a value of 1.15 A while i_2 and i_3 almost identically decrease by about 38%, dipping to 410 mA.

Overall, the effectiveness of our MIMO control has been validated numerically on a full-scale scenario. The same scenario has been tested with a real-time HIL setup. Finally, a scaled-down prototype has confirmed that the proposed control architecture effectively meets the expected performance.

VII. Conclusion

A new MIMO control for dc–dc interleaved buck converters in EV dc fast charging applications was presented in this brief. The proposed control avoids multiple tuning of controllers in multiple and interconnected loops, improving, at the same time, the dynamical behavior of the converter with respect to standard PI/PID regulators. The results of our simulations have confirmed that the tracking error vanishes monotonically from any initial state of the battery charge, and under reference current step and load variations. Moreover, the proposed control is shown to compensate for imbalances among the legs due to either different parasitic resistances or dissimilar aging of the components. The proposed control framework has been experimentally tested to validate the theoretical and simulated analysis utilizing full-scale HIL and scaled-down setups.

Future developments are aimed at achieving a current balancing action without the use of a dedicated transducer if a sensor-less approach through estimators is carried out [32].

References

[1] R. G. Retegui, M. Benedetti, M. Funes, P. Antoszczuk, and D. Carrica, "Current control for high-dynamic high-power multiphase buck converters," *IEEE Trans. Power Electron.*, vol. 27, no. 2, pp. 614–618, Feb. 2012.

[2] O. Garcia, P. Zumel, A. de Castro, and J. A. Cobos, "Automotive DC–DC bidirectional converter made with many interleaved buck stages," *IEEE Trans. Power Electron.*, vol. 21, no. 3, pp. 578–586, May 2006.

[3] X. Zhou, P. Xu, and F. C. Lee, "A novel current-sharing control technique for low-voltage high-current voltage regulator module applications," *IEEE Trans. Power Electron.*, vol. 15, no. 6, pp. 1153–1162, Nov. 2000.

[4] D. Schumacher, P. Magne, M. Preindl, B. Bilgin, and A. Emadi, "Closed loop control of a six phase interleaved bidirectional DC–DC boost converter for an EV/HEV application," in *Proc. IEEE Transp. Electrific. Conf. Expo (ITEC)*, Jun. 2016, pp. 1–7.

[5] L. Ni, D. J. Patterson, and J. L. Hudgins, "High power current sensorless bidirectional 16-phase interleaved DC–DC converter for hybrid vehicle application," *IEEE Trans. Power Electron.*, vol. 27, no. 3, pp. 1141–1151, Mar. 2012.

[6] G. Balen, A. R. Reis, H. Pinheiro, and L. Schuch, "Modeling and control of interleaved buck converter for electric vehicle fast chargers," in *Proc. Brazilian Power Electron. Conf. (COBEP)*, Nov. 2017, pp. 1–6.

[7] H.-C. Chen, C.-Y. Lu, and U. S. Rout, "Decoupled master-slave current balancing control for three-phase interleaved boost converters," *IEEE Trans. Power Electron.*, vol. 33, no. 5, pp. 3683–3687, May 2018.

[8] S. Cuoghi, R. Mandrioli, L. Ntogramatzidis, and G. Gabriele, "Multileg interleaved buck converter for EV charging: Discrete-time model and direct control design," *Energies*, vol. 13, no. 2, p. 466, Jan. 2020.

[9] K. E. L. Marcillo et al., "Interval robust controller to minimize oscillations effects caused by constant power load in a DC multi-converter buck-buck system," *IEEE Access*, vol. 7, pp. 26324–26342, 2019.

[10] M. H. Mahmud, Y. Zhao, and Y. Zhang, "A sliding mode duty-ratio control with current balancing algorithm for interleaved buck converters," in *Proc. IEEE Appl. Power Electron. Conf. Exposit. (APEC)*, Mar. 2018, pp. 2281–2287.

[11] M. Leso, J. Zilkova, and P. Girovsky, "Development of a simple fuzzy logic controller for DC–DC converter," in *Proc. IEEE 18th Int. Power Electron. Motion Control Conf. (PEMC)*, Aug. 2018, pp. 86–93.

[12] R. Schmid and L. Ntogramatzidis, "A unified method for the design of nonovershooting linear multivariable state-feedback tracking controllers," *Automatica*, vol. 46, no. 2, pp. 312–321, Feb. 2010.

[13] L. Ntogramatzidis, J.-F. Trégouët, R. Schmid, and A. Ferrante, "Globally monotonic tracking control of multivariable systems," *IEEE Trans. Autom. Control*, vol. 61, no. 9, pp. 2559–2564, Sep. 2016.

[14] J. M. Blanes, R. Gutiérrez, A. Garrigós, J. L. Lizán, and J. M. Cuadrado, "Electric vehicle battery life extension using ultracapacitors and an FPGA controlled interleaved buck-boost converter," *IEEE Trans. Power Electron.*, vol. 28, no. 12, pp. 5940–5948, Dec. 2013.

[15] *Electric Vehicles From Life Cycle and Circular Economy Perspectives*, Eur. Environ. Agency, Copenhagen, Denmark, 2018.

[16] M. Y. Metwly, M. S. Abdel-Majeed, A. S. Abdel-Khalik, R. A. Hamdy, M. S. Hamad, and S. Ahmed, "A review of integrated on-board EV battery chargers: Advanced topologies, recent developments and optimal selection of FSCW slot/pole combination," *IEEE Access*, vol. 8, pp. 85216–85242, 2020.

[17] M. Yilmaz and P. T. Krein, "Review of battery charger topologies, charging power levels, and infrastructure for plug-in electric and hybrid vehicles," *IEEE Trans. Power Electron.*, vol. 28, no. 5, pp. 2151–2169, May 2013.

[18] W.-S. Lee, J.-H. Kim, J.-Y. Lee, and I.-O. Lee, "Design of an isolated DC/DC topology with high efficiency of over 97% for EV fast chargers," *IEEE Trans. Veh. Technol.*, vol. 68, no. 12, pp. 11725–11737, Dec. 2019.

[19] K. Drobnic et al., "An output ripple-free fast charger for electric vehicles based on grid-tied modular three-phase interleaved converters," *IEEE Trans. Ind. Appl.*, vol. 55, no. 6, pp. 6102–6114, Nov. 2019.

[20] J. Channegowda, V. K. Pathipati, and S. S. Williamson, "Comprehensive review and comparison of DC fast charging converter topologies: Improving electric vehicle plug-to-wheels efficiency," in *Proc. IEEE 24th Int. Symp. Ind. Electron. (ISIE)*, Jun. 2015, pp. 263–268.

[21] S. Rivera, B. Wu, S. Kouro, V. Yaramasu, and J. Wang, "Electric vehicle charging station using a neutral point clamped converter with bipolar DC bus," *IEEE Trans. Ind. Electron.*, vol. 62, no. 4, pp. 1999–2009, Apr. 2015.

[22] Y. Gao, X. Zhang, Q. Cheng, B. Guo, and J. Yang, "Classification and review of the charging strategies for commercial lithium-ion batteries," *IEEE Access*, vol. 7, pp. 43511–43524, 2019.

[23] M. S. H. Lipu et al., "Review of electric vehicle converter configurations, control schemes and optimizations: Challenges and suggestions," *Electronics*, vol. 10, no. 4, p. 477, Feb. 2021.

[24] F. Lo Franco, M. Ricco, R. Mandrioli, A. Viatkin, and G. Grandi, "Current pulse generation methods for li-ion battery chargers," in *Proc. 2nd IEEE Int. Conf. Ind. Electron. Sustain. Energy Syst. (IESES)*, Sep. 2020, pp. 339–344.

[25] G.-J. Chen, Y.-H. Liu, Y.-S. Cheng, and H.-Y. Pai, "A novel optimal charging algorithm for lithium-ion batteries based on model predictive control," *Energies*, vol. 14, no. 8, p. 2238, Apr. 2021.

[26] Y. He, B. M. Chen, and C. Wu, "Composite nonlinear control with state and measurement feedback for general multivariable systems with input saturation," *Syst. Control Lett.*, vol. 54, no. 5, pp. 455–469, May 2005.

[27] N. How, M. A. Hannan, M. S. Hossain Lipu, and P. J. Ker, "State of charge estimation for lithium-ion batteries using model-based and data-driven methods: A review," *IEEE Access*, vol. 7, pp. 136116–136136, 2019.

[28] J. Meng et al., "An overview and comparison of online implementable SOC estimation methods for lithium-ion battery," *IEEE Trans. Ind. Appl.*, vol. 54, no. 2, pp. 1583–1591, Mar./Apr. 2018.

[29] S. Cuoghi and L. Ntogramatzidis, "Inversion formulae for the design of PIDF controllers," in *Proc. 4th Austral. Control Conf. (AUCC)*, Nov. 2014, pp. 140–145.

[30] S. Li and B. Ke, "Study of battery modeling using mathematical and circuit oriented approaches," in *Proc. IEEE Power Energy Soc. Gen. Meeting*, Jul. 2011, pp. 1–8.

[31] F. Lo Franco et al., "Electric vehicles charging management system for optimal exploitation of photovoltaic energy sources considering vehicle-to-vehicle mode," *Frontiers Energy Res.*, vol. 9, Nov. 2021, Art. no. 716389.

[32] A. Viatkin, M. Ricco, R. Mandrioli, T. Kerekes, R. Teodorescu, and G. Grandi, "Sensorless current balancing control for interleaved half-bridge submodules in modular multilevel converters," *IEEE Trans. Ind. Electron.*, vol. 70, no. 1, pp. 5–16, Jan. 2023.

Open Access funding provided by 'Alma Mater Studiorum - Università di Bologna' within the CRUI CARE Agreement